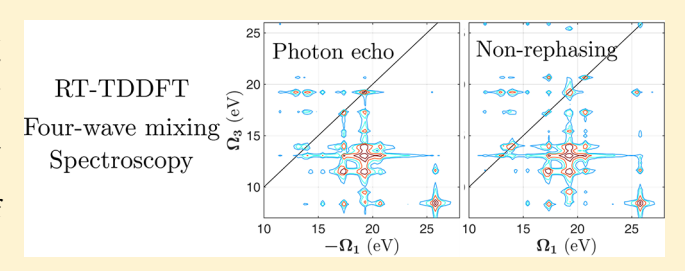
## Phase Cycling RT-TDDFT Simulation Protocol for Nonlinear XUV and X-ray Molecular Spectroscopy

Daeheum Cho,\*\*,†,†,¶® Jérémy R. Rouxel,†,¶ Markus Kowalewski,†,¶® Prasoon Saurabh,†,¶ Jin Yong Lee,\*,†,® and Shaul Mukamel\*,†,¶®

Supporting Information

ABSTRACT: Real-time time-dependent density functional theory (RT-TDDFT) provides a practical algorithm for propagating a many-electron system driven by external laser fields. The fields are included nonperturbatively in the propagation, and the molecular reduced single-electron density operator and various spectroscopic and diffraction signals can be computed directly, avoiding the expensive calculation of many-body states. Nonlinear optical signals contain contributions of multiple pathways. A phase cycling protocol is



implemented in order to separate these pathways. Simulations of XUV four-wave mixing signals in the CO molecule are compared with ab initio sum-over-states calculations.

Multidimensional nonlinear spectroscopy has become an indispensable tool for probing molecular structure, structural/ electronic dynamics, energy transfer, and chemical reactions. 1-9 Useful information on the couplings between molecular degrees of freedom (spin, vibrational, or electronic) can be obtained by disentangling a congested one-dimensional spectrum into *n*-dimensions by scanning the interpulse delays. Spreading the linear absorption spectrum in multidimensions allows one to monitor and unravel the dynamics of, e.g., intermolecular energy transfer processes in molecular aggregates. Intense ultrashort pulses are needed to monitor subfemtosecond electronic processes. Recently developed XUV and X-ray light sources can monitor electronic dynamics in real time with attosecond temporal resolution.

Nonlinear signals are given by sums over Liouville pathways, each representing a distinct history of the molecular density matrix. Phase matching is a conventional tool for distinguishing various pathways. 10 This scheme uses a noncollinear pulse configuration, and signals corresponding to different groups of pathways are then emitted in different directions that can be detected separately. Desired signals can be extracted by the direction of the signal field, which for third order techniques is  $\mathbf{k}_{s} = \pm \mathbf{k}_{1} \pm \mathbf{k}_{2} \pm \mathbf{k}_{3}$ , where  $\mathbf{k}_{1}$ ,  $\mathbf{k}_{2}$ , and  $\mathbf{k}_{3}$  are the wave vectors of the incoming fields.

Phase cycling is an alternative way to separate various pathways by employing collinear pulses with different phases. 6,11-16 Measurements are repeated for a finite set of phase differences between the incoming pulses  $\phi_s = \pm \phi_1 \pm \phi_2$  $\pm \phi_3$ , where  $\phi_1$ ,  $\phi_2$ , and  $\phi_3$  are the phases of the incoming fields. The contributions of different groups of pathways can be singled out from the total polarization by proper summations over signals with different polarization configurations.

Multidimensional signals are commonly simulated by the sum-over-states (SOS) technique, in which the signal is calculated from electronic eigenstates and the coupling to electric fields, which is treated perturbatively under the dipole approximation. Nonlinear signals are calculated from corresponding matter quantities: transition dipoles, transition energies, and dephasing rates.

An alternative approach for computing multidimensional signals is to simulate the electronic dynamics by propagating the reduced one-electron density matrix driven by multiple electric fields, 17 avoiding the explicit calculation of manyelectron eigenstates. Nonlinear effects induced by intense external fields can be described because the incoming fields are treated nonperturbatively. Numerous methods such as time-dependent Hartree–Fock, 18 time-dependent density functional theory (TDDFT), <sup>19</sup> coupled cluster, <sup>20</sup> and multiconfigurational self-consistent field calculations<sup>21</sup> have been developed for calculating excited states. In this Letter, we use real-time timedependent density functional theory (RT-TDDFT). 19,22-24 This technique has been broadly applied to compute absorption spectra of large molecules, 25 core ionization dynamics, 6 charge transfer, 27,28 light absorption of photocatalysts, 9 molecular conductance, 30 and ultrafast charge migration following ionization in a peptide.<sup>31</sup> We further

Received: January 8, 2018 Accepted: February 12, 2018 Published: February 12, 2018

<sup>&</sup>lt;sup>†</sup>Department of Chemistry, University of California, Irvine, California 92697, United States

<sup>\*</sup>Department of Chemistry, Sungkyunkwan University, Suwon 16419, Korea

Department of Physics and Astronomy, University of California, Irvine, California 92697, United States

implement the phase cycling protocol to extract desired nonlinear signals from a finite set of RT-TDDFT simulations for multiple incoming fields with variable phases.

We present the phase cycling scheme for four-wave mixing (FWM) signals. The RT-TDDFT simulations are carried out to compute XUV and X-ray nonlinear signals for the CO molecule. The results are compared with complete active space self-consistent field SOS (CASSCF-SOS) calculations.

Phase Cycling Protocol for Four-Wave Mixing Signals. In thirdorder nonlinear FWM spectroscopy,  $^{6,32}$  the system interacts with three electric pulses  $\mathbf{E}_i(t)$ , where  $i \in \{1, 2, 3\}$  indicates the order of arrival of the pulses, and is finally detected by the local oscillator field  $\mathbf{E}_4(t)$  that interferes with the emitted signal to result in heterodyne detection. Figure 1 shows (a) the pulse

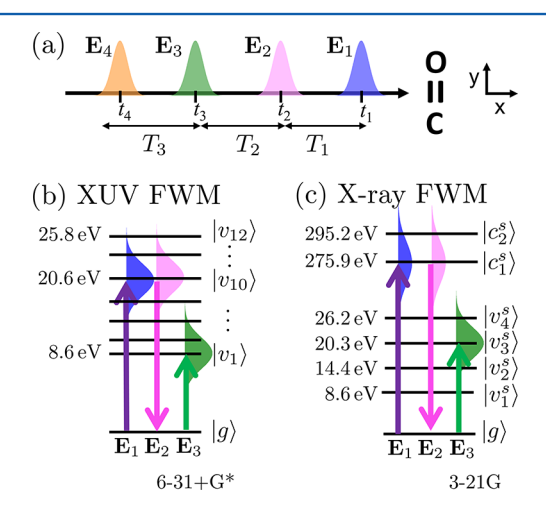


Figure 1. (a) Pulse sequence for FWM. All fields are x-polarized. Relevant (b) XUV and (c) X-ray level schemes for CO calculated at LR-TDDFT/PBE0/6-31+G\* and 3-21G, respectively; ground state  $|v_n^{(s)}\rangle$ , valence states  $|v_n^{(s)}\rangle$ , and carbon K-edge states  $|c_n^{(s)}\rangle$  (superscript s indicates the energy levels calculated with 3-21G basis set.). The electronic transitions triggered by the incoming electric fields  $E_1$ ,  $E_2$ , and  $E_3$  are indicated by arrows with bandwidths. See Figure S1 for corresponding Liouville pathway diagrams.

scheme, time delays, and relevant levels covered by the (b) XUV and (c) X-ray pulse bandwidths for FWM spectroscopy of CO. The reduced single-electron density matrix  $\rho(t)$  dynamics is obtained by solving the TDDFT equations of motion 17

$$i\frac{\partial\rho(t)}{\partial t} = [\mathbf{F}(t), \rho(t)] \tag{1}$$

(in au), where F(t) is the time-dependent Fock matrix in which the interaction between the system and the optical field in the dipole approximation is described.<sup>33</sup> The resulting single-electron density matrix then allows one to calculate the expectation value of all single-body operators such as the dipole  $\langle \mu(t) \rangle$  and the charge density  $\langle \sigma(\mathbf{r}, t) \rangle$ . The heterodyne detected signal is then given by

$$S = \Im \int dt \langle \boldsymbol{\mu}(t) \rangle \cdot \mathbf{E}_4^*(t)$$
 (2)

In the RT-TDDFT protocol, eq 1 is integrated numerically nonperturbatively in the field, and the signal in eq 2 contains contributions from all interaction pathways to all orders in the fields.

We next show how the third-order contribution and desired pathways can be singled out from the total RT-TDDFT signal. The third-order signal  $S^{(3)}$  is given by

$$S^{(3)}(t_3, t_2, t_1) = \int dt dt_3 dt_2 dt_1 R^{(3)}(t_3, t_2, t_1)$$

$$\times \mathbf{E}_4(t)\mathbf{E}_3(t - t_3)\mathbf{E}_2(t - t_3 - t_2)\mathbf{E}_1(t - t_3 - t_2 - t_1)$$
(3)

The third-order response function  $R^{(3)}(t_3, t_2, t_1)$  can be expanded in Liouville pathways (see Supporting Information Figure S1 for diagrams)

$$R^{(3)}(t_3, t_2, t_1) = \sum_{n=1}^{6} R_n(t_3, t_2, t_1) + \text{c.c.}$$
(4)

Pathways 1, 2, and 3 represent the photon echo signal ( $\mathbf{k}_{\mathrm{I}} = -\mathbf{k}_{\mathrm{I}} + \mathbf{k}_{\mathrm{2}} + \mathbf{k}_{\mathrm{3}}$ ) with phase  $\phi_{\mathrm{I}} = -\phi_{\mathrm{1}} + \phi_{\mathrm{2}} + \phi_{\mathrm{3}} - \phi_{\mathrm{4}}$ , while 4, 5, and 6 represent nonrephasing signals ( $\mathbf{k}_{\mathrm{II}} = \mathbf{k}_{\mathrm{1}} - \mathbf{k}_{\mathrm{2}} + \mathbf{k}_{\mathrm{3}}$ ) with phase  $\phi_{\mathrm{II}} = \phi_{\mathrm{1}} - \phi_{\mathrm{2}} + \phi_{\mathrm{3}} - \phi_{\mathrm{4}}$ . The double quantum coherence signals ( $\mathbf{k}_{\mathrm{III}} = \mathbf{k}_{\mathrm{1}} + \mathbf{k}_{\mathrm{2}} - \mathbf{k}_{\mathrm{3}}$ ) with phase  $\phi_{\mathrm{III}} = \phi_{\mathrm{1}} + \phi_{\mathrm{2}} - \phi_{\mathrm{3}} - \phi_{\mathrm{4}}$  are not considered in this Letter because they involve doubly excited states, which cannot be adequately described by TDDFT.

The entire third-order signal can be recast as

$$S^{(3)}(\phi_{1}, \phi_{2}, \phi_{3}, \phi_{4}) = \sum_{n=1}^{6} e^{i(\pm\phi_{1}\pm\phi_{2}\pm\phi_{3}-\phi_{4})} \int dt dt_{3} dt_{2} dt_{1} R_{n}(t_{3}, t_{2}, t_{1})$$

$$\times \mathbf{E}_{4}(t)\mathbf{E}_{3}(t-t_{3})\mathbf{E}_{2}(t-t_{3}-t_{2})\mathbf{E}_{1}(t-t_{3}-t_{2}-t_{1})$$

$$= \sum_{n=1}^{6} c_{n}(\phi_{1}, \phi_{2}, \phi_{3}, \phi_{4})S_{n}$$
(5)

where n is an index for the third-order response functions representing the different Liouville pathway

$$S_n = \Im \int dt dt_3 dt_2 dt_1 R_n(t_3, t_2, t_1) \mathbf{E}_4(t) \mathbf{E}_3(t - t_3)$$

$$\times \mathbf{E}_2(t - t_3 - t_2) \mathbf{E}_1(t - t_3 - t_2 - t_1)$$
(6)

and

$$c_{1}(\phi_{1}, \phi_{2}, \phi_{3}, \phi_{4}) = e^{i(-\phi_{1} + \phi_{2} + \phi_{3} - \phi_{4})}$$

$$c_{4}(\phi_{1}, \phi_{2}, \phi_{3}, \phi_{4}) = e^{i(\phi_{1} - \phi_{2} + \phi_{3} - \phi_{4})}$$
(7)

The photon echo diagrams,  $R_1$ ,  $R_2$ , and  $R_3$ , share the same overall phase  $\phi_I = -\phi_1 + \phi_2 + \phi_3 - \phi_4$  and then  $c_1 = c_2 = c_3$ , whereas the nonrephasing diagrams,  $R_4$ ,  $R_5$ , and  $R_6$ , have the phase  $\phi_{II} = +\phi_1 - \phi_2 + \phi_3 - \phi_4$  and then  $c_4 = c_5 = c_6$ . The photon echo  $R_I$  and nonrephasing  $R_{II}$  response functions are given by

$$R_{\rm I} = R_1 + R_2 + R_3$$
  $R_{\rm II} = R_4 + R_5 + R_6$  (8)

For third-order response functions, a four-step phase cycling protocol is sufficient to separate  $R_{\rm I}$  and  $R_{\rm II}^{\ \ 10}$ 

$$S_{XXX}^{(3)} \propto + \Re R_{\rm I} + \Re R_{\rm II} \tag{9}$$

$$S_{XYX}^{(3)} \propto -\Im R_{\rm I} + \Im R_{\rm II} \tag{10}$$

$$S_{XYY}^{(3)} \propto +\Re R_{\rm I} - \Re R_{\rm II} \tag{11}$$

$$S_{XXY}^{(3)} \propto + \Im R_{\rm I} + \Im R_{\rm II} \tag{12}$$

where  $S_{\phi_1,\phi_2,\phi_3}^{(3)}$  is a third-order signal with phases  $\phi_1$ ,  $\phi_2$ , and  $\phi_3$ , and X=0,  $Y=\pi/2$ , and  $Z=\pi$ . We then have

The Journal of Physical Chemistry Letters

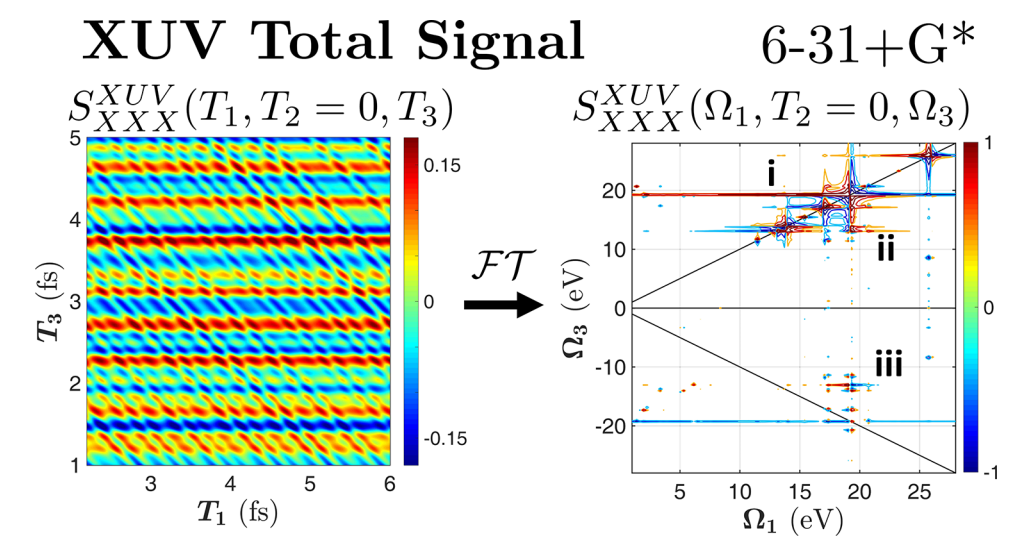


Figure 2. 2D Fourier transform ( $\mathcal{FT}$ ) of dipole moment  $S_{XXX}^{XUV}(T_1, T_2 = 0, T_3)$  (left panel) gives the 2D correlation spectrum  $S_{XXX}^{XUV}(\Omega_1, T_2 = 0, \Omega_3)$  (right panel) for XUV excitations of CO calculated at the PBE0/6-31+G\* level.

$$R_{\rm I} \propto S_{\rm XXX}^{(3)} + S_{\rm XYY}^{(3)} - i\{S_{\rm XYX}^{(3)} - S_{\rm XXY}^{(3)}\}$$
 (13)

$$R_{\rm II} \propto S_{XXX}^{(3)} - S_{XYY}^{(3)} + i\{S_{XYX}^{(3)} + S_{XXY}^{(3)}\}$$
 (14)

This protocol, however, does not eliminate lower-order signals (from first  $R^{(1)}$  and second  $R^{(2)}$  order response functions), and a phase cycling with additional phase combinations is needed. We have used a nine-step phase cycling protocol with  $\phi_1 = X$ ,  $\phi_2 \in \{X, Y, Z\}$ ,  $\phi_3 \in \{X, Y, Z\}$ , and  $\phi_4 = X$ . By solving a set of linear equations of the signals listed in Supporting Information Table S1 with a set of phase combinations, we can distinguish the photon echo  $\mathbf{k}_{\mathrm{I}}$  and nonrephasing  $\mathbf{k}_{\mathrm{II}}$  signals from lower-order signals. The real and imaginary parts of photon echo  $R_{\mathrm{I}}$  and nonrephasing  $R_{\mathrm{II}}$  response functions can be obtained by relating the phase cycling coefficients matrix and total signals with a different set of phase combinations  $S_{\phi_1,\phi_2,\phi_3}$  (see Supporting Information eq S1).

RT-TDDFT Simulation of Four-Wave Mixing Signals. We have employed RT-TDDFT as implemented in NWChem<sup>33,34</sup> to simulate FWM signals resonant with the valence and/or carbon K-edge coherence in the CO molecule. The PBE0<sup>35</sup> exchange correlation functional was used in the closed-shell calculations. The 1D time-dependent dipole moment (Figure S3) and absorption spectra (Figure S4) were calculated with various basis sets to test the basis set effect: 3-21G, 6-31G\*, 6-31+G\*, 6-311+G\*, and aug-cc-pVDZ (aVDZ). We found that the inclusion of diffuse functions is critical to describe both valence and core excitations of CO by comparing the 6-31G\* and 6-31+G\*. The 6-31+G\* and 3-21G basis sets were used for XUV FWM spectroscopy, while 3-21G was used for X-ray FWM spectroscopy due to the high computational cost for simulating the ultrafast X-ray coherences. The total simulation times for the real-time propagation are 1500 au = 36.3 fs and 1000 au = 24.2 fs for XUV and X-ray FWM spectroscopies, respectively. A  $\Delta t = 0.1$  au (2.42 as) time step was used to simulate the XUV FWM signals, and a shorter  $\Delta t = 0.02$  au (0.48 as) time step was used to simulate X-ray FWM signals in order to capture the coherences created by X-ray pulses. Linear-response TDDFT (LR-TDDFT) calculations employing the PBE0 functional were performed to provide energy levels of valence excited states of CO (Figure 1b). Restricted excitation window

TDDFT (REW-TDDFT)<sup>36</sup> employing PBE0 functional calculations provided the energy levels of carbon K-edge states of CO (Figure 1c). Complete active space self-consistent field SOS (CASSCF-SOS) calculations with the 3-21G basis set and full valence active space were performed with MOLPRO<sup>37</sup> for XUV FWM signals in order to confirm the phase cycling results obtained from RT-TDDFT.

XUV Signals. We have simulated XUV FWM signals generated by four XUV pulses. Figure 1b shows the relevant valence levels of CO covered by the XUV pulse bandwidths: ground  $|g\rangle$  and valence  $|\nu_n\rangle$  states. The first two pulses (E<sub>1</sub> and  $E_2$ ) are resonant with  $|\nu_{10}\rangle$  ( $|\nu_3^{\rm s}\rangle$  for 3-21G), i.e.,  $\omega_1=\omega_2=20.3$ eV and  $\sigma_1 = \sigma_2 = 0.2$  fs (fwhm of 8.8 eV) (see eq 15). The third pulse (E<sub>3</sub>) was set resonant with  $|\nu_1\rangle$ , i.e.,  $\omega_3 = 8.6$  eV with  $\sigma_3 =$ 0.2 fs (fwhm of 8.8 eV). The local oscillator field ( $\mathbf{E}_{4}$ ) was taken as a delta function in time and was not included explicitly in the simulation. Heterodyne detection records the signals selected by the convolution with the local oscillator field. The 2D FWM signals were obtained by scanning the delays  $T_1$  and  $T_3$ , keeping  $T_2 = 0$ .  $T_1$  was varied from 2.2 to 17 fs with 10 as increments to cover the 200 eV spectral region in  $\Omega_1$  with 0.28 eV spectral resolution.  $T_3$  was scanned between 1.0 and 18 fs with 2.4 as the time step to yield a 0.24 eV spectral resolution and 850 eV spectral range in  $\Omega_3$ . The 2D correlation spectrum ( $S(\Omega_1, T_2 =$  $(0, \Omega_3)$ ) in the frequency domain is calculated by 2D FT of the 2D dipole moment  $(S(T_1, T_2 = 0, T_3))$  with respect to the  $T_3$ and  $T_1$  delays. We assumed a Gaussian electric field envelope

$$\mathbf{E}_{i}(t) = A \sin(\omega_{i}(t - t_{i}) + \phi_{i}) \exp[-(t - t_{i})^{2}/(2\sigma_{i}^{2})]$$
(15)

with an electric field strength of A = 0.01 au =  $3.51 \times 10^{14}$  W/cm² for all incoming fields, central time  $t_{ij}$  central frequency  $\omega_{ij}$  pulse duration  $\sigma_{ij}$  and phase  $\phi_{i}$ . Time delays between pulses are given by  $T_i = t_{i+1} - t_i$ . All fields are x-polarized (see Figure 1 for the axes' definition).

Figure 2 shows the total signal  $S_{XXX}^{XUV}$ , which contains all orders in the incoming fields (see Supporting Information Figure S7 for different phase combinations). Intense linear absorption from coherences between ground and valence states  $(|\nu_n\rangle\langle g|)$  created by  $\mathbf{k}_s=\mathbf{k}_1$  interaction show up along the diagonal (i). Weaker second-order  $(\mathbf{k}_s=\mathbf{k}_1-\mathbf{k}_2)$  or  $\mathbf{k}_s=\mathbf{k}_1$ 

# XUV FWM Signals 6-31+G\*

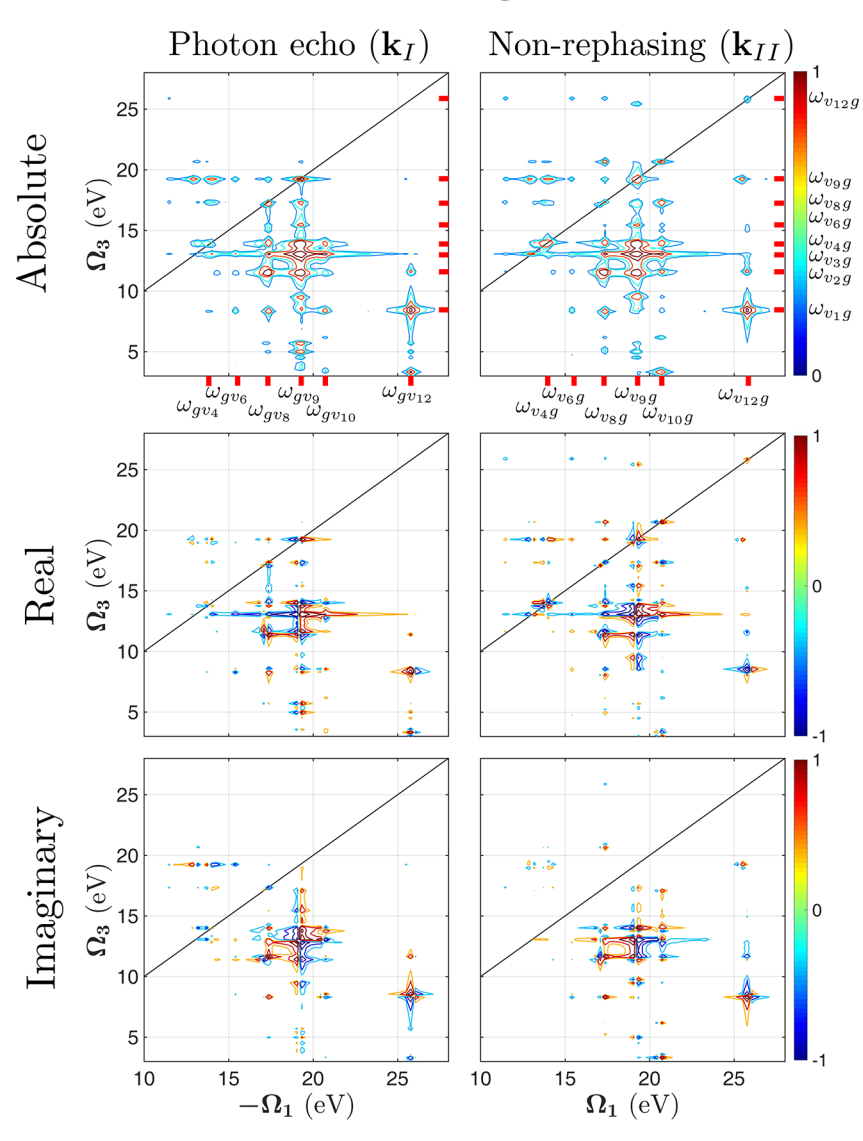


Figure 3. Absolute value (top), real (middle), and imaginary (bottom) parts of (left panel) photon echo  $R_1 = R_1 + R_2 + R_3$  and (right panel) nonrephasing  $R_{II} = R_4 + R_5 + R_6$  response functions for XUV excitations of CO calculated at the PBE0/6-31+G\* level, obtained by the nine-step phase cycling protocol.

 $k_3$ ) and third-order nonrephasing signals  $k_{II}$  are off-diagonal in the  $(+\Omega_1 + \Omega_3)$  quadrant (ii). The other second-  $(\mathbf{k}_s = -\mathbf{k}_1 + \mathbf{k}_2)$ or  $\mathbf{k}_s = -\mathbf{k}_1 + \mathbf{k}_3$ ) and third-order photon echo  $\mathbf{k}_I$  signals are offdiagonal in the  $(-\Omega_1 + \Omega_3)$  quadrant (iii) (the complex conjugate value is shown in the Figure 2). These are located in a similar spectral region for  $\omega_1 = \omega_2 = 20.3$  eV and  $\omega_3 = 8.6$ eV. The phase cycling protocol was employed to select the desired  $k_I$  and  $k_{II}$  signal out of the total signals. The phase cycling protocol is required to disentangle (1) the FWM signal from lower-order signals and (2) the photon echo  $k_I$  and nonrephasing  $k_{II}$  signals. The first-order signals do not depend on the phase differences among the three incoming fields due to the fixed phase of the  $\mathbf{E}_1$  ( $\phi_1 = X$ ) for all phase combinations (Supporting Information Figure S7). The second- and thirdorder signals, on the other hand, vary according to the phase differences. We exploit these variations in the phase cycling protocol.

Figure 3 shows the absolute value and the real and the imaginary parts of third-order response functions, photon echo  $R_{\rm I}$  and nonrephasing  $R_{\rm II}$ , obtained by the nine-point phase cycling protocol (eq S1). Cross-peak intensities reflect correlations among the valence excited states. The FWM signals are assigned as correlations among  $|\nu_1\rangle - |\nu_{12}\rangle$ . Strong correlations were found between  $|\nu_8\rangle/|\nu_9\rangle/|\nu_{10}\rangle$  and  $|\nu_2\rangle/|\nu_3\rangle/|\nu_4\rangle$  and  $|\nu_{12}\rangle$  and  $|\nu_1\rangle$ . This may indicate that significant ultrafast charge migration from the former to the latter could take place within the time scale of ~36 fs. The peak positions exactly match the linear response TDDFT results.

Comparison between CASSCF-SOS/3-21G and RT-TDDFT/PBE0/3-21G shown in Figures S5 and S6 in the Supporting Information confirms the RT-TDDFT results, except for the double excitations of  $|\nu_1\rangle$  appearing in the  $\Omega_1$  =  $\pm 17-18$  eV range in the CASSCF-SOS result. This discrepancy may be due to the well-known inability of TDDFT to describe a multideterminant wave function or the

The Journal of Physical Chemistry Letters

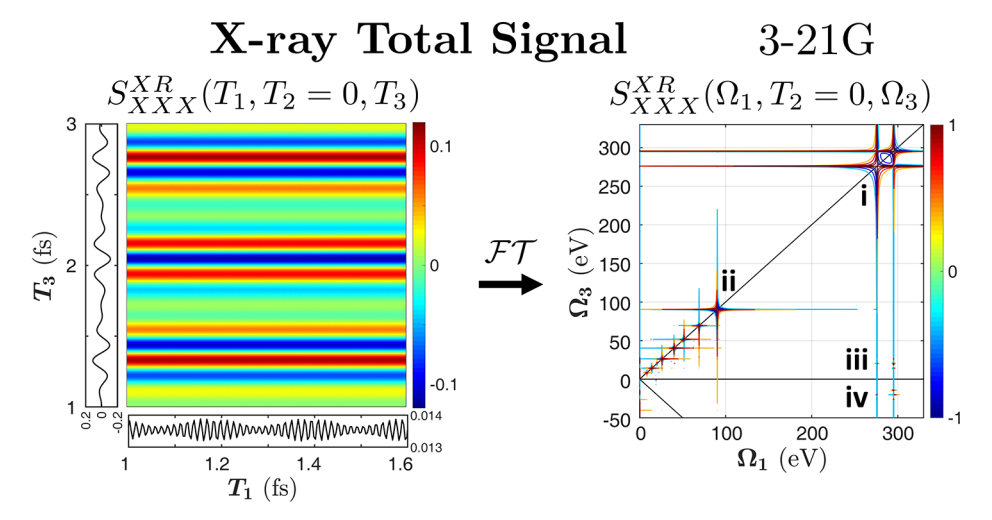


Figure 4. 2D Fourier transform ( $\mathcal{FT}$ ) of  $S_{XXX}^{XR}(T_1, T_2 = 0, T_3)$  (left panel) gives the 2D correlation spectrum  $S_{XXX}^{XR}(\Omega_1, T_2 = 0, \Omega_3)$  (right panel) for X-ray excitations of CO calculated at the PBE0/3-21G level.

small basis set 3-21G. Further study is required to address this issue. The XUV FWM signals reveal the coherences between valence excited states and the ultrafast charge migration.

Mixed X-ray/XUV Signals. We have further simulated the FWM signals generated by two X-ray and two XUV pulses. The first two pulses ( $\mathbf{E}_1$  and  $\mathbf{E}_2$ ) are resonant with  $|c_1^s\rangle$ , i.e.,  $\omega_1 = \omega_2$ = 275.9 eV with a  $\sigma_1 = \sigma_2 = 11$  as pulse duration (fwhm of 26 as) (eq 15). The third pulse ( $E_3$ ) is resonant with the  $|\nu_3^s\rangle$ absorption, i.e.,  $\omega_3 = 20.3$  eV with a  $\sigma_3 = 0.2$  fs pulse duration (fwhm of 8.8 eV).  $T_1$  was scanned from 0.8 to 10 fs in 4 as increments to yield the 500 eV spectral region in  $\Omega_1$  with spectral resolution of 0.45 eV. T<sub>3</sub> was scanned between 1 and 13 fs with 0.48 as increments to yield a 0.32 eV spectral resolution and 4000 eV spectral range in  $\Omega_3$ . The energy levels of C K-edge states are underestimated by ~10 eV (Figure 1c) from the experiment (fundamental band at 287 eV), and the 1h-1e peak is missing due to the small 3-21G basis set (see Figure S4 for the effect of the basis sets).<sup>38</sup> However, it is common to shift the computed C K-edge excitation energy by about 10 eV in order to match the experimental value within the TDDFT framework.<sup>36</sup> Moreover, mixed X-ray/XUV FWM signals presented here provide the insight on the correlations between C K-edge and valence states of CO.

Figure 4 depicts the total signals  $S_{XXX}^{XR}$  containing the contributions to all orders. The total signals with different phase combinations are presented in the Supporting Information Figure S8. The first-order (linear absorption) signals generate strongest peaks along the diagonal line. The first X-ray pulse  $(E_1)$  excites the 275 and 290 eV carbon K-edge (C 1s core) states (i in Figure 4, right panel). The  $E_1$  pulse also excites the system to the valence states regime (ii in Figure 4) due to broad excitation pulse bandwidths (fwhm of 140 eV). Second-order signals are also shown with a much weaker intensity than the first-order signals. Second-order cross-peaks between the two core states  $|c_1^s\rangle$  and  $|c_2^s\rangle$  are masked by intense linear absorption from the core states (i in Figure 4). Correlation peaks in the valence regime are distinguishable from the linear absorption (ii). The third-order photon echo  $\mathbf{k}_{I}$ and nonrephasing k<sub>II</sub> signals are marked iv and iii, respectively, in the figure. These are masked by the intense carbon K-edge linear absorption. The FWM signals are assigned by the correlation between  $|c_1^s\rangle$  and  $|c_2^s\rangle$  for the  $E_1$  excitation and  $|\nu_2^s\rangle$ ,

 $|\nu_3^s\rangle$ , and  $|\nu_4^s\rangle$  for the simultaneous de-excitation of carbon K-edge states by  $E_2$  and excitation of valence states by  $E_3$  pulses.

Figure 5 depicts the third-order response functions, photon echo  $R_{\rm I}$  and nonrephasing  $R_{\rm II}$ , obtained by the nine-step phase cycling protocol (eq S1). FWM signals are generated by  $|g\rangle\langle c_n^s|$ (or  $|c_n^s\rangle\langle g|$ ) coherence during  $T_1$  and  $|\nu_n^s\rangle\langle g|$  or  $|\nu_m^s\rangle\langle \nu_n^s|$ coherences during  $T_3$ . Significant correlation peaks between I  $|c_1^s\rangle/|c_2^s|$  and  $|v_2^s\rangle/|v_3^s\rangle/|v_4^s\rangle$  indicate ultrafast charge migration from the core to valence states and ultimately trigger the subsequent charge transfer or nuclear dynamics. Simulations of a similar X-ray FWM signal with a larger basis such as 6-31+G\* could resolve the correlations between the core and valence states in detail with higher accuracy. The signals from the  $|\nu_n^s\rangle\langle g|$  coherences are much stronger than those from  $|\nu_m^s\rangle\langle \nu_n^s|$ . Mixed X-ray/XUV FWM signals reveal the coherences between core and valence excited states and ultimately how the ultrafast charge migration takes place from the core to valence states. This information could be used to understand how the charge migration initiated by X-ray pulses triggers the subsequent charge transfer or nuclear fragmentation dynamics involving the XUV excited states.

We have employed the phase cycling protocol to simulate third-order optical signals, photon echo and nonrephasing, from lower-order signals obtained by the total signal from a finite set of RT-TDDFT simulations under multiple incoming fields with different phase combinations. The 2D correlation spectra were obtained by 2D FT of the time-evolving dipole moments calculated by RT-TDDFT. A nine-step phase cycling protocol was used to separate photon echo and nonrephasing response functions from lower-order signals. Correlations between relevant electronic excited states created by the incoming fields can be extracted from the 2D spectra. Peak positions calculated by RT-TDDFT simulation exactly match linear response TDDFT results. Comparison with CASSCF-SOS calculations confirms the RT-TDDFT results, except for the double excitations. This may due to the inability of TDDFT to describe a multideterminant wave function or the use of a small basis set. Real-time propagation of the reduced singleelectron density matrix driven by the incoming fields allows one to simulate multidimensional nonlinear signals in a nonperturbative manner, in contrast to a conventional perturbative SOS method based on the response functions.

# X-ray FWM Signals 3-21G

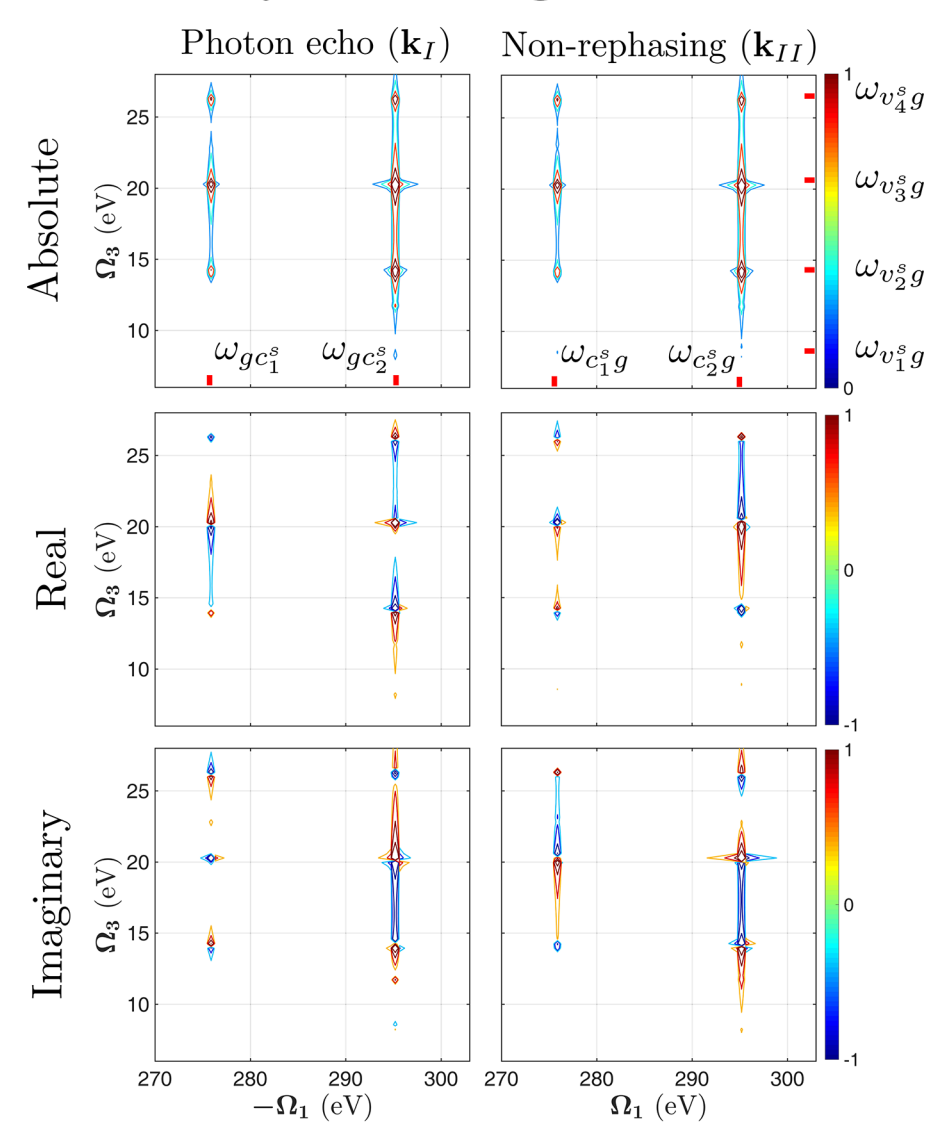


**Figure 5.** Absolute value (top), real (middle), and imaginary (bottom) parts of (a) photon echo  $R_1 = R_1 + R_2 + R_3$  and (b) nonrephasing  $R_{II} = R_4 + R_5 + R_6$  response functions from X-ray excitation of CO calculated at the PBE0/3-21G level, obtained by the nine-step phase cycling protocol.

#### ASSOCIATED CONTENT

### **S** Supporting Information

The Supporting Information is available free of charge on the ACS Publications website at DOI: 10.1021/acs.jpclett.8b00061.

- (1) Phase cycling protocol for four-wave mixing signals,
- (2) effect of the basis set, (3) comparison between CASSCF-SOS and RT-TDDFT FWM signals, and (4) total signals from XUV and X-ray excitations with different phase combinations (PDF)

### AUTHOR INFORMATION

#### **Corresponding Authors**

\*E-mail: daeheumc@uci.edu (D.C.).

\*E-mail: jinylee@skku.edu (J.Y.L.).

\*E-mail: smukamel@uci.edu (S.M.).

#### ORCID ®

Daeheum Cho: 0000-0002-0322-4291 Markus Kowalewski: 0000-0002-2288-2548 Jin Yong Lee: 0000-0003-0360-5059 Shaul Mukamel: 0000-0002-6015-3135

#### Notes

The authors declare no competing financial interest.

#### ACKNOWLEDGMENTS

The support of the Chemical Sciences, Geosciences, and Biosciences Division, Office of Basic Energy Sciences, Office of Science, U.S. Department of Energy through Award No. DE-FG02-04ER15571 and of the National Science Foundation (Grant No. CHE-1663822) is gratefully acknowledged. J.R.R. was supported by the DOE grant.

#### REFERENCES

- (1) Mukamel, S. Principles of Nonlinear Optical Spectroscopy; Oxford University Press, 1995.
- (2) Mukamel, S. Multidimensional Femtosecond Correlation Spectroscopies of Electronic and Vibrational Excitations. *Annu. Rev. Phys. Chem.* **2000**, *51*, 691–729.

- (3) Jonas, D. M. Two-Dimensional Femtosecond Spectroscopy. *Annu. Rev. Phys. Chem.* **2003**, *54*, 425–463.
- (4) Hochstrasser, R. M. Two-dimensional spectroscopy at infrared and optical frequencies. *Proc. Natl. Acad. Sci. U. S. A.* **2007**, *104*, 14190–14196.
- (5) Cho, M. Coherent two-dimensional optical spectroscopy. *Chem. Rev.* **2008**, *108*, 1331–1418.
- (6) Gelin, M. F.; Egorova, D.; Domcke, W. Efficient Calculation of Time- and Frequency-Resolved Four-Wave-Mixing Signals. *Acc. Chem. Res.* **2009**, 42, 1290–1298.
- (7) Gelin, M. F.; Egorova, D.; Domcke, W. Manipulating electronic couplings and nonadiabatic nuclear dynamics with strong laser pulses. *J. Chem. Phys.* **2009**, *131*, 124505.
- (8) Cao, W.; Warrick, E. R.; Fidler, A.; Leone, S. R.; Neumark, D. M. Near-resonant four-wave mixing of attosecond extreme-ultraviolet pulses with near-infrared pulses in neon: Detection of electronic coherences. *Phys. Rev. A: At., Mol., Opt. Phys.* **2016**, *94*, 21802.
- (9) Calegari, F.; Ayuso, D.; Trabattoni, A.; Belshaw, L.; de Camillis, S.; Anumula, S.; Frassetto, F.; Poletto, L.; Palacios, A.; Decleva, P.; Greenwood, J. B.; Martín, F.; Nisoli, M. Ultrafast electron dynamics in phenylalanine initiated by attosecond pulses. *Science* **2014**, *346*, 336–339.
- (10) Hamm, P.; Zanni, M. Concepts and Methods of 2D Infrared Spectroscopy; Cambridge University Press: Cambridge, 2011.
- (11) Keusters, D.; Tan, H. S.; Warren, W. S. Role of pulse phase and direction in two-dimensional optical spectroscopy. *J. Phys. Chem. A* **1999**, *103*, 10369–10380.
- (12) Tian, P.; Keusters, D.; Suzaki, Y.; Warren, W. S. Femtosecond Phase-Coherent Two-Dimensional Spectroscopy. *Science* **2003**, *300*, 1553—1555.
- (13) Scheurer, C.; Mukamel, S. Design strategies for pulse sequences in multidimensional optical spectroscopies. *J. Chem. Phys.* **2001**, *115*, 4989–5004.
- (14) Scheurer, C.; Mukamel, S. Magnetic Resonance Analogies in Multidimensional Vibrational Spectroscopy. *Bull. Chem. Soc. Jpn.* **2002**, 75, 989–999.
- (15) Shim, S.-H.; Zanni, M. T. How to turn your pump-probe instrument into a multidimensional spectrometer: 2D IR and Vis spectroscopiesvia pulse shaping. *Phys. Chem. Chem. Phys.* **2009**, *11*, 748–761.
- (16) Yan, S.; Tan, H. S. Phase cycling schemes for two-dimensional optical spectroscopy with a pump-probe beam geometry. *Chem. Phys.* **2009**, *360*, 110–115.
- (17) Tretiak, S.; Mukamel, S. Density Matrix Analysis and Simulation of Electronic Excitations in Conjugated and Aggregated Molecules. *Chem. Rev.* **2002**, *102*, 3171–3212.
- (18) Kulander, K. C. Time-dependent Hartree-Fock theory of multiphoton ionization: Helium. *Phys. Rev. A: At., Mol., Opt. Phys.* **1987**, *36*, 2726–2738.
- (19) Runge, E.; Gross, E. K. U. Density-Functional Theory for Time-Dependent Systems. *Phys. Rev. Lett.* **1984**, *52*, 997–1000.
- (20) Nascimento, D. R.; DePrince, A. E. Simulation of Near-Edge X-ray Absorption Fine Structure with Time-Dependent Equation-of-Motion Coupled-Cluster Theory. *J. Phys. Chem. Lett.* **2017**, *8*, 2951–2957.
- (21) Meyer, H.-D.; Manthe, U.; Cederbaum, L. S. The multiconfigurational time-dependent Hartree approach. *Chem. Phys. Lett.* **1990**, *165*, 73–78.
- (22) Yabana, K.; Bertsch, G. F. Time-dependent local-density approximation in real time. *Phys. Rev. B: Condens. Matter Mater. Phys.* **1996**, *54*, 4484–4487.
- (23) Kosloff, R. Time-dependent quantum-mechanical methods for molecular dynamics. *J. Phys. Chem.* **1988**, *92*, 2087–2100.
- (24) Castro, A.; Marques, M. A. L.; Rubio, A. Propagators for the time-dependent Kohn-Sham equations. *J. Chem. Phys.* **2004**, *121*, 3425–3433.
- (25) Tussupbayev, S.; Govind, N.; Lopata, K.; Cramer, C. J. Comparison of Real-Time and Linear-Response Time-Dependent Density Functional Theories for Molecular Chromophores Ranging

- from Sparse to High Densities of States. J. Chem. Theory Comput. 2015, 11, 1102-1109.
- (26) Bruner, A.; Hernandez, S.; Mauger, F.; Abanador, P. M.; LaMaster, D. J.; Gaarde, M. B.; Schafer, K. J.; Lopata, K. Attosecond Charge Migration with TDDFT: Accurate Dynamics from a Well-Defined Initial State. *J. Phys. Chem. Lett.* **2017**, *8*, 3991–3996.
- (27) Petrone, A.; Lingerfelt, D. B.; Rega, N.; Li, X. From charge-transfer to a charge-separated state: a perspective from the real-time TDDFT excitonic dynamics. *Phys. Chem. Chem. Phys.* **2014**, *16*, 24457–24465.
- (28) Peng, B.; Lingerfelt, D. B.; Ding, F.; Aikens, C. M.; Li, X. Real-Time TDDFT Studies of Exciton Decay and Transfer in Silver Nanowire Arrays. *J. Phys. Chem. C* **2015**, *119*, 6421–6427.
- (29) Govind, N.; Lopata, K.; Rousseau, R.; Andersen, A.; Kowalski, K. Visible Light Absorption of N-Doped TiO2 Rutile Using (LR/RT)-TDDFT and Active Space EOMCCSD Calculations. *J. Phys. Chem. Lett.* **2011**, 2, 2696–2701.
- (30) Cheng, C.-L.; Evans, J. S.; Van Voorhis, T. Simulating molecular conductance using real-time density functional theory. *Phys. Rev. B: Condens. Matter Mater. Phys.* **2006**, 74, 155112.
- (31) Cho, D.; Rouxel, J. R.; Kowalewski, M.; Lee, J. Y.; Mukamel, S. Attosecond X-ray Diffraction Triggered by Core or Valence Ionization of a Dipeptide. *J. Chem. Theory Comput.* **2018**, *14*, 329.
- (32) Gelin, M. F.; Egorova, D.; Domcke, W. Efficient method for the calculation of time- and frequency-resolved four-wave mixing signals and its application to photon-echo spectroscopy. *J. Chem. Phys.* **2005**, 123, 164112.
- (33) Lopata, K.; Govind, N. Modeling Fast Electron Dynamics with Real-Time Time-Dependent Density Functional Theory: Application to Small Molecules and Chromophores. *J. Chem. Theory Comput.* **2011**, *7*, 1344–1355.
- (34) Valiev, M.; Bylaska, E. J.; Govind, N.; Kowalski, K.; Straatsma, T. P.; Van Dam, H. J. J.; Wang, D.; Nieplocha, J.; Apra, E.; Windus, T. L.; de Jong, W. A. NWChem: A comprehensive and scalable open-source solution for large scale molecular simulations. *Comput. Phys. Commun.* **2010**, *181*, 1477–1489.
- (35) Adamo, C.; Barone, V. Toward reliable density functional methods without adjustable parameters: The PBE0 model. *J. Chem. Phys.* **1999**, *110*, 6158–6170.
- (36) Lopata, K.; van Kuiken, B. E.; Khalil, M.; Govind, N. Linear-Response and Real-Time Time-Dependent Density Functional Theory Studies of Core-Level Near-Edge X-Ray Absorption. *J. Chem. Theory Comput.* **2012**, *8*, 3284–3292.
- (37) Werner, H.-J.; Knowles, P. J.; Knizia, G.; Manby, F. R.; Schütz, M.; Celani, P.; Györffy, W.; Kats, D.; Korona, T.; Lindh, R.; Mitrushenkov, A.; Rauhut, G.; Shamasundar, K. R.; Adler, T. B.; Amos, R. D.; Bernhardsson, A.; Berning, A.; Cooper, D. L.; Deegan, M. J. O.; Dobbyn, A. J.; Eckert, F.; Goll, E.; Hampel, C.; Hesselmann, A.; Hetzer, G.; Hrenar, T.; Jansen, G.; Köppl, C.; Liu, Y.; Lloyd, A. W.; Mata, R. A.; May, A. J.; McNicholas, S. J.; Meyer, W.; Mura, M. E.; Nicklass, A.; O'Neill, D. P.; Palmieri, P.; Peng, D.; Pflüger, K.; Pitzer, R.; Reiher, M.; Shiozaki, T.; Stoll, H.; Stone, A. J.; Tarroni, R.; Thorsteinsson, T.; Wang, M. MOLPRO, version 2015.1, a package of ab initio programs; 2015.
- (38) Domke, M.; Xue, C.; Puschmann, A.; Mandel, T.; Hudson, E.; Shirley, D. A.; Kaindl, G. Carbon and oxygen K-edge photoionization of the CO molecule. *Chem. Phys. Lett.* **1990**, *173*, 122–128.